Journal of Operation and Automation in Power Engineering
Vol. XX, No. XX, XXXX, Pages: XXXX (Proofed)
http://joape.uma.ac.ir

Research Paper

A Novel Simplified Protection Algorithm for Multi-Terminal HVDC Systems Using Travelling Wave-Based Modified Frequency-Spectrum Hilbert Transform

Ehsan Akbari *

Department of Electrical Engineering, Mazandaran University of Science and Technology, Babol, Iran.

Abstract— *High-voltage direct current (HVDC) transmission systems in multi-terminal configurations are prone to faults due to their structural complexity and multiple power-carrying branches. A failure in such systems may propagate fault waveforms, causing damage to other branches and interconnected networks. To prevent this, accurate and fast protection schemes are required for fault detection, classification, section identification, and location estimation. Traveling wave (TW) theory has been widely applied as a rapid protection method due to its simplicity in implementing complex structures. However, its accuracy decreases under noise and frequency disturbances. This paper proposes a modified frequency spectrum Hilbert transform (MFSHT)-based TW protection scheme that compensates for frequency disturbance errors in conventional Hilbert spectrum analysis. Voltage signals are measured at multiple points in the HVDC grid and processed by the protection algorithm. Simulation results demonstrate that the proposed scheme achieves 100% accuracy in fault detection, classification, and section identification, with an average fault-location error of less than 0.2%. Sensitivity analyses and comparative studies further confirm its effectiveness and superiority.*

Keywords—Multi-terminal high voltage direct current system, fault detection, classification, section determination and location estimation, travelling wave theory.

1. INTRODUCTION

High-voltage direct current (HVDC) transmission networks in multi-terminal configurations are highly vulnerable to faults because of their numerous branches and structural complexity. Accurate and rapid identification of the faulty segment is essential to prevent fault propagation to other branches and interconnected AC networks [1]. Existing protection models for multi-terminal HVDC systems mainly rely on the traveling wave (TW) theory. However, these models often show reduced accuracy in fault detection due to sensitivity to wave speed and the arrival times of traveling waves at system terminals [2]. To address this issue, learning-based approaches have been developed and have shown promising results [3]. Methods such as adaptive neuro-fuzzy inference system (ANFIS) [4], neural networks (NN) [5], and support vector machines (SVM) [6] have been widely used for two-terminal HVDC protection. Yet, as the number of terminals increases, these approaches face major challenges, including higher computational burden, longer response times, large training dataset requirements, and the need for multiple protection levels (detection, classification, section identification, and location) [7].

Received: 09 Feb. 2025
Revised: 26 Sept. 2025
Accepted: 01 Nov. 2025
*Corresponding author:
E-mail: e.akbari@ustmb.ac.ir (E. Akbari)
DOI: 10.22098/joape.2025.16764.2298

Therefore, the most effective strategy for achieving both speed and accuracy in multi-terminal HVDC protection is to enhance traditional TW-based models by modifying their signal processing stages [8]. Signal processing techniques are commonly used to extract the temporal features of traveling waves for fault location in transmission networks [9–11]. In general, mathematical transforms applied to fault signals can be grouped into time-domain transforms [12] and time–frequency transforms [13]. Time–frequency transforms such as the wavelet transform (WT) [14], Gabor transform (GT) [15], short-time Fourier transform (STFT) [16], Hilbert–Huang transform (HHT) [17], and Stockwell transform (ST) [18] have been widely used for fault detection, classification, and location. Despite their accuracy, these methods impose heavy computational demands, making them less suitable for large-scale multi-terminal HVDC networks.

In contrast, time-domain transforms are simpler and more computationally efficient, as they analyze the raw time-domain features of fault signals (e.g., differentiation, integration, and peak detection) [19]. Although these methods enable fast implementation, their accuracy decreases in complex MTHVDC networks where noise and system dynamics distort fault signals. Thus, the challenge lies in balancing computational efficiency with the accuracy required for reliable protection. This has led to growing interest in improving time-domain methods or hybridizing them with other techniques to achieve both precision and speed in MTHVDC protection [20].

In this paper, we propose a simple, computationally efficient, and accurate protection scheme for fault detection, classification, section identification, and location in multi-terminal HVDC systems. The method is based on a modified frequency spectrum Hilbert transform (MFSHT). Voltage signals measured at different points in the system are first processed by the Hilbert transform to obtain their instantaneous frequency spectrum. After spectrum correction, features are extracted for further analysis. To reduce the effects of electromagnetic coupling between the positive and negative poles, the signals are decoupled using the Karrenbauer transform. The 1-mode voltage component is then applied for fault detection and section identification, while the positive- and negative-pole voltages are used for fault classification and location estimation.

The proposed method performs all four protection functions using only voltage signals. Unlike previous approaches that rely on trial-and-error thresholds, this study introduces an adaptive thresholding scheme based on fault spectrum characteristics. The main benefits of the proposed scheme are high speed, low computational burden, no need for prior system data, no requirement for simultaneous voltage–current measurements, and independence from combined signal processing methods such as EMD–HT [21] or LMD–HT [22]. A comparison of the related state-of-the-art methods and their respective contributions is presented in Table 1.

The key contributions of this work are summarized as follows:

- A new time-domain protection method for multi-terminal HVDC lines is presented, capable of performing detection, classification, section identification, and location estimation in a unified framework.
- An adaptive thresholding mechanism is introduced to improve fault detection accuracy and reliability.
- The method is scalable and can be generalized to n-terminal HVDC systems.
- The scheme relies only on measured voltage signals, eliminating the need for additional system information or current measurements.

The remainder of the paper is structured as follows: Section 2 presents the proposed model, Section 3 provides the simulation results, Section 4 discusses sensitivity analysis, Section 5 presents a comprehensive sensitivity analysis, Section 6 provides a comparative study with existing methods, Section 7 discusses the findings and research limitations, and finally, Section 8 concludes the paper with a summary of the main results.

2. THE PROPOSED PROTECTION ALGORITHM

All protection models based on the traveling wave (TW) theory operate by analyzing the arrival times of propagating waves at the measurement points. The accuracy in extracting these arrival times directly affects the performance and reliability of the protection scheme. In a typical three-terminal HVDC system, as shown in Fig. 1, these time components are indicated. By measuring the initial voltage signals at the terminals and processing them through the protection algorithm, these time components can be precisely extracted. Subsequently, using traveling wave theory, the fault location for each section can be estimated.

2.1. Hilbert Transform (HT)

In this paper, the proposed modified frequency spectrum Hilbert transform (MFSHT) is applied to process the measured voltage signals. The MFSHT is a time-domain mathematical transform that extracts the analytic signal from a real-valued time-domain signal. It has widespread applications in signal processing, communications, and related fields, including envelope detection, modulation analysis, and phase estimation. The Hilbert transform of a signal $x(t)$ is a linear operator that produces a new signal, $\hat{x}(t)$, representing the quadrature component of the original signal, i.e., a 90° phase-shifted version. Mathematically, it is defined as follows:

$$\hat{x}(t) = H\left\{x(t)\right\} = \frac{1}{\pi}\sum\nolimits_{-\infty}^{\infty}\frac{x(\tau)}{t-\tau}d\tau \tag{1}$$

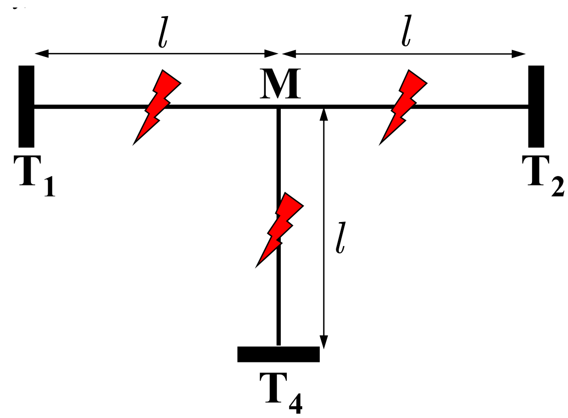

Fig. 1. Three-terminal HVDC system.

Here, the integral is evaluated as a Cauchy principal value to account for the singularity at $t = \tau$. The analytic signal is a complex-valued representation of the real signal $x(t)$, defined as:

$$\tilde{x}(t) = x(t) + j\hat{x}(t) \tag{2}$$

Here, j denotes the imaginary unit, and $\hat{x}(t)$ represents the Hilbert transform of $x(t)$. The analytic signal $\tilde{x}(t)$ has the original real signal $x(t)$ as its real part and the Hilbert transform $\hat{x}(t)$ as its imaginary part. This representation captures both the instantaneous amplitude and phase of the signal, providing a complete description. Such a representation is particularly useful in applications including fault detection, modulation analysis, and general signal processing. From the analytic signal $\tilde{x}(t)$, the instantaneous amplitude and phase can be extracted as follows:

$$\begin{aligned} A(t) &= |\tilde{x}(t)| = \sqrt{x^2(t) + \hat{x}^2(t)} \\ \phi(t) &= arg(\tilde{x}(t)) = tan^{-1}\tfrac{\hat{x}(t)}{x(t)} \end{aligned} \tag{3}$$

For a real-valued signal $x(t)$, the instantaneous frequency is defined as the time derivative of the instantaneous phase $\phi(t)$.

$$f_{inst}(t) = \frac{1}{2\pi}\frac{d\phi(t)}{dt} \tag{4}$$

It can be observed from Eq. (4) that the instantaneous frequency, derived through the Hilbert transform, depends on the time derivative, allowing for the determination of the frequency distribution at each moment. By computing the instantaneous frequency corresponding to each voltage signal, its temporal characteristics can be effectively extracted. Moreover, instantaneous frequency serves as a critical parameter for fault detection, fault section identification, and faulted phase determination. To improve the accuracy of conventional HT-based methods, a frequency modification mechanism is incorporated.

2.2. Frequency modification algorithm

To improve the performance of the Hilbert transform approach, this study introduces a frequency modification algorithm. This algorithm refines the instantaneous frequency spectrum while preserving the flexibility and adaptability required for fault detection in non-stationary signals. After computing the initial instantaneous frequency via the Hilbert transform, the frequency components are further decomposed using an adaptive filter or wavelet packet decomposition (WPD) to isolate fault-related components. A detailed description of WPD can be found in [23].

$$f_{dom}(t) = WPD\left(f_{inst}(t)\right) \tag{5}$$

Table 1. Comparative summary of state-of-the-art protection schemes and their key contributions.

Ref.	Method / Approach	Domain	Main advantages	Limitations / Challenges
[4]	ANFIS	AI-based	Good nonlinear mapping	Training complexity; scalability issues
[5]	Neural Networks (NN)	AI-based	High fault detection accuracy	Long training, risk of overfitting, large datasets needed
[6]	Support Vector Machines (SVM)	AI-based	Robust classification	Not scalable to large n-terminal systems; dataset dependent
[14]	Wavelet Transform (WT)	Time–frequency	Good localization of transient features	Heavy computational demand
[15]	Transient Extracting Transform (TET)	Time–frequency	Accurate transient extraction	High complexity, not real-time friendly
[16]	Short-Time Fourier Transform (STFT)	Time–frequency	Simple, well-known	Poor resolution trade-off, high computation
[17]	Hilbert–Huang Transform (HHT)	Time–frequency	Adaptive, high accuracy	Mode-mixing issues, expensive computation
[18]	Stockwell Transform (ST)	Time–frequency	Frequency-dependent resolution	Heavy computation, unsuitable for real-time
[21]	EMD–HT	Hybrid	Good accuracy	Complex, requires iterative decomposition
[22]	LMD–HT	Hybrid	Improved accuracy over EMD–HT	Still computationally heavy
This work	**Modified Frequency Spectrum Hilbert Transform (MFSHT)**	**Time-domain (spectrum corrected)**	**Fast, low complexity, no prior data, voltage-only, adaptive threshold, scalable to n-terminals**	**New method; requires further validation on field data**

In the next step, an initial weighting function $W(f)$ is defined with equal importance assigned to all frequency components. During successive iterations, the weighting function is updated according to the significance of each frequency component. Subsequently, an adaptive filter is applied to refine the instantaneous frequency $f_{inst}(t)$ as follows:

$$f_{filtered}^{(n)}(t) = W^{(n)}\left(f_{inst}(t)\right).f_{inst}(t) \tag{6}$$

where $W^{(n)}$ represents the weighting function at the n-th iteration. Following this step, the analytic signal is reconstructed using the modified instantaneous frequency.

$$\begin{aligned} &x_{refined}^{(n)}(t) = \\ &A(t).\exp j2\pi \textstyle\sum_0^t f_{filtered}^{(n)}(\tau)\, d\tau \end{aligned} \tag{7}$$

In the next phase, the instantaneous frequency spectrum is updated by extracting the instantaneous frequency of the refined signal.

$$f_{refined}^{(n)}(t) = \frac{1}{2\pi}\frac{d}{dt}\arg\left(x_{refined}^{(n)}(t)\right) \tag{8}$$

In iteration $n+1$, the weighting function is updated according to the following equation:

$$\begin{aligned} &W^{(n+1)}(f) = W^{(n)}(f) + \\ &\eta.\left|f_{refined}^{(n)}(t) - f_{dom}(t)\right| \end{aligned} \tag{9}$$

where η denoted the learning rate controlling the adaptation speed. Finally, the differential frequency is computed using Eq. (10), and the stopping condition of the frequency correction algorithm is evaluated based on $\Delta f(n) < \Delta f_{thr}$. Here, Δf_{thr} is a predefined threshold determined according to the frequency characteristics of the fault.

$$\Delta f^{(n)} = \frac{\left\| f_{refined}^{(n)}(t) - f_{refined}^{(n-1)}(t) \right\|}{\left\| f_{refined}^{(n)}(t) \right\|} \tag{10}$$

By modifying the Hilbert transform (HT) frequency spectrum using the proposed algorithm, the temporal characteristics of the traveling waves are identified with higher accuracy. These time characteristics, together with the peak values of the modified instantaneous frequency, are then used in the implementation of the protection algorithm. The following subsections present a detailed description of each step involved in the proposed protection scheme.

2.3. Fault detection scheme

To detect a fault in the MTHVDC system using the proposed algorithm, voltage signals measured at the network terminals are required. At this stage, measuring the voltage at the interconnection node is not necessary. The voltage components recorded at the positive and negative terminals are processed using the Karrenbauer transform to extract the 1-mode voltage component for each terminal, as expressed by the following equation:

$$\begin{bmatrix} V_0 \\ V_1 \end{bmatrix} = \frac{\sqrt{2}}{2}\begin{bmatrix} 1 & 1 \\ 1 & -1 \end{bmatrix}\begin{bmatrix} V_p \\ V_n \end{bmatrix} \tag{11}$$

where V_p and V_n represent the voltages measured at the positive and negative pole terminals, respectively, and V_1 denotes the 1-mode voltage component used for fault detection and section identification in this study. To implement this, the maximum values of the instantaneous frequency spectra, obtained via the proposed HT algorithm with frequency modification, are compared against a predefined threshold for each terminal. If at least one maximum value exceeds the threshold, a fault is detected. It is noteworthy that the threshold value is computed based on the method described in Section 2.7.

2.4. Faulted section determination scheme

Similar to the previous subsection, the 1-mode voltage component is used to identify the faulted section(s). In this step, the maximum value of the instantaneous frequency spectrum at each terminal is compared with the threshold determined by the proposed model in Section 2.7. The sections where the maximum frequency value at the corresponding terminals exceeds the threshold are identified as the faulted sections of the network.

2.5. Fault classification scheme

To classify faults in the MTHVDC network, the voltage components measured at the positive and negative poles of the faulty terminals must be analyzed separately. This approach allows for identifying the possible fault types, including positive pole-to-ground (PTG), negative pole-to-ground (NTG), and positive pole-to-negative pole (PTN) faults.

After determining the faulty section, the positive and negative pole voltages at the terminal connected to the affected section are processed using the proposed algorithm to obtain their respective instantaneous frequency spectra. If the fault occurs on a single pole (PTG or NTG), the difference between the peak values of the instantaneous frequency spectra (IFSPV) for V_p and V_n is significant. In contrast, for a PTN fault, this difference is minimal or close to zero. To quantify this distinction, the differential index E_{pn} is defined as follows:

$$E_{pn} = \left| IFSPV_{V_p} - IFSPV_{V_n} \right| \tag{12}$$

If E_{pn} is greater than ε, a pole-to-ground (PTG or NTG) fault is identified. Otherwise, the fault is classified as a positive pole-to-negative pole (PTN) fault. To further distinguish between PTG and NTG faults, the following condition must be evaluated:

$$\begin{cases} if\ IFSPV_{V_p} > IFSPV_{V_n}, & Fault\ Type = PTG \\ \quad else, & Fault\ Type = NTG \end{cases} \tag{13}$$

2.6. Fault location estimation scheme

To estimate the fault location within the faulted section, the voltage components at both ends of the positive and negative poles of the affected section are required. Specifically, if a fault occurs at terminal k, which is connected to interconnection node $k-1$, the voltages V_{p_k},V_{N_k},$V_{p_{k-1}}$, and $V_{N_{k-1}}$ must be analyzed. If the fault is classified as a pole-to-ground (PTG or NTG) fault, only the voltage components of the faulted pole are used in the TW-based fault location algorithm. However, if the fault involves both poles (PTN fault), all four voltage components are incorporated into the algorithm. For example, assuming a fault occurs in the section connected to terminal k, the fault location is estimated using the following equations, depending on the classified fault type:

- For PTG fault:

$$\hat{d} = \frac{v \times \left(t\left(FSPV_{V_{p_k}}\right) - t\left(FSPV_{V_{p_{k-1}}}\right)\right) + l}{2} \tag{14}$$

- For NTG fault:

$$\hat{d} = \frac{v\left[t\Big(FSPV_{V_{N_k}}\Big) - t\Big(FSPV_{V_{N_{k-1}}}\Big)\right] + l}{2} \tag{15}$$

- For PTN fault:

$$\hat{d} = \frac{v\,\Delta t_{\text{actual}} + l}{2} \tag{16}$$

$$\begin{cases} \Delta t_p = t\left(FSPV_{V_{P_k}}\right) - t\left(FSPV_{V_{P_{k-1}}}\right) \\ \Delta t_n = t\left(FSPV_{V_{N_k}}\right) - t\left(FSPV_{V_{N_{k-1}}}\right) \end{cases} \tag{17}$$

In these equations, l represents the length of the transmission line between nodes k and $k-1$, while v denotes the wave propagation velocity. The wave propagation velocity is given by $\frac{1}{\sqrt{LC}}$, where L and C indicate the total inductance and capacitance of the transmission line, respectively.

These equations highlight that fault location estimation based on traveling wave theory is highly dependent on the accurate determination of wavefront arrival times at the measurement points within the network. Therefore, a precise method for identifying these arrival times is essential. The proposed algorithm effectively extracts these time components by analyzing the frequency spectrum of the measured voltages. Furthermore, thanks to the frequency spectrum modification, the performance of the proposed protection scheme is enhanced across all stages, including fault detection, classification, and section identification.

2.7. Threshold value computation scheme

To resolve ambiguities in traditional threshold value calculation methods—which often rely on trial and error and the simulation of multiple scenarios—this study proposes an adaptive threshold model based on fault characteristics. Conventional approaches are sensitive to variations in fault parameters, such as impedance and fault type, which can adversely affect the accuracy of fault detection. The proposed adaptive model overcomes these limitations by dynamically determining the threshold value according to fault characteristics, thereby ensuring improved reliability and robustness. In this model, two statistical measures—energy (E) and root mean square (RMS)—are computed based on the numerical differences between consecutive samples in the instantaneous frequency spectrum of the 1-mode voltage at all network terminals. The ratio of these two measures is then defined as the threshold value. Consequently, if the frequency spectrum contains m samples, the resulting differential frequency spectrum vector, denoted as Δx_{IF} (see Eq. (18)), will have $m-1$ components due to the one-sample delay.

$$\Delta x_{IF} = |x_{IF}(t) - x_{IF}(t+T_s)| \tag{18}$$

where T_s represents the sampling period. Fig. 2 illustrates the procedure for calculating Δx_{IF} for an arbitrary frequency spectrum at the moment of fault occurrence. After computing the Δx_{IF} vector, its energy and RMS values are determined, and this procedure is repeated for all network terminals. Subsequently, the threshold value is defined as the ratio of the total energy across all terminals to the total RMS values, as expressed in the following equation:

$$\text{Thr}_{IF_{(k,i)}} = \frac{1}{n}\left(\frac{\sum_{k=1}^{n}\sum_{i=1}^{m-1}\left|\Delta x_{IF_{(k,i)}}\right|^2}{\sqrt{\frac{\sum_{k=1}^{n}\sum_{i=1}^{m-1}\left|\Delta x_{IF_{(k,i)}}\right|^2}{4}}} \right) = \frac{1}{2}\left(\frac{E_{\Delta x_{IF_{(k,i)}}}}{RMS_{\Delta x_{IF_{(k,i)}}}} \right) \tag{19}$$

In this equation, n represents the number of network terminals, while m denotes the number of recorded samples of the 1-mode voltage signal, determined according to the sampling rate.

Consequently, the threshold value is adaptively computed in real time, with a delay equivalent to one sampling period, based on the fault characteristics. This adaptive approach enhances the sensitivity of the fault detection model to variations in fault parameters, thereby improving its overall accuracy and reliability. Finally, the flowchart of the proposed protection algorithm is illustrated in Fig. 3.

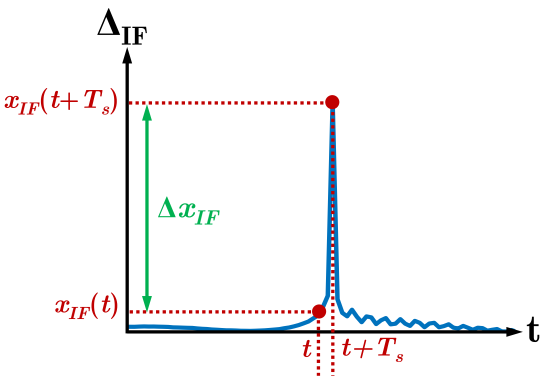

Fig. 2. The calculation method of Δx_{IF} for an arbitrary frequency spectrum at the moment of fault occurrence.

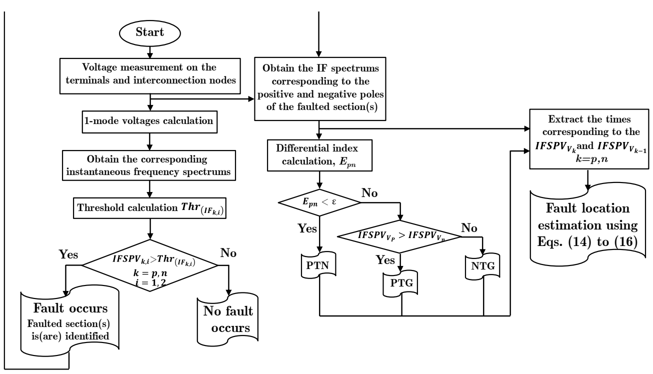

Fig. 3. Flowchart of the proposed protection model.

As illustrated in Fig. 3, the proposed protection algorithm begins with the measurement of terminal voltages in the multi-terminal HVDC network. These signals are first processed through the Karrenbauer transform to extract the 1-mode voltage component, which minimizes the influence of pole coupling. The Hilbert transform is then applied to obtain the instantaneous frequency spectrum, followed by the frequency modification stage that refines fault-related features. Using this corrected spectrum, the occurrence of a fault is detected once the maximum instantaneous frequency exceeds an adaptively calculated threshold. In the next stage, the section in which the threshold is violated is identified as the faulted line. To determine the fault type, the positive- and negative-pole voltage components are analyzed: a differential index distinguishes between pole-to-ground and pole-to-pole faults. Finally, the fault location is estimated based on the corrected wavefront arrival times, while the adaptive thresholding mechanism continuously updates the decision boundary in real time to ensure robustness against variations in fault type, impedance, and operating conditions.

3. SIMULATION RESULTS

To validate the proposed protection scheme, a three-terminal HVDC system is simulated in the MATLAB/Simulink environment, as illustrated in Fig. 4, and tested under various fault scenarios. The simulated system parameters and predefined characteristics of the protection scheme are presented in Table 2.

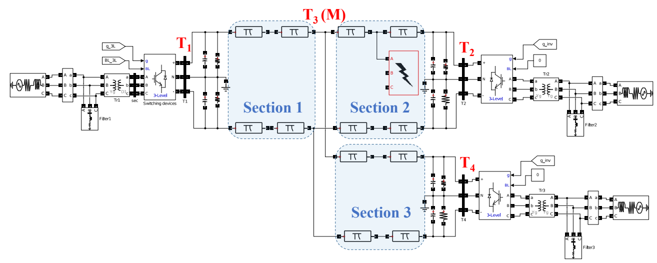

Fig. 4. Simulated three-terminal HVDC system.

Table 2. Simulation parameters.

Parameter	Symbol	Value
Transmission line length per section	l	100 km
Line inductance	L	30×10^{-6} H/km
Line capacitance	C	50×10^{-9} F/km
AC grid rated voltage	V	50 kV
AC grid rated power	S	200 MVA
AC grid frequency	f	50 Hz
Threshold value for the differential index E_{pn}	ε	1 Hz
Stopping criterion of the frequency modification algorithm	Δf_{thr}	0.01 Hz
Sampling rate	T_s	1×10^{-4} s

Although the proposed scheme is validated on a three-terminal 50 kV HVDC system, it is applicable to HVDC systems with different voltage levels, line lengths, and transmission capacities, as the algorithm adapts to system-specific wave propagation characteristics and utilizes an adaptive threshold for fault detection and localization.

3.1. PTG fault scenario on Section 1 at a distance of d=65 km

In this subsection, a PTG fault is simulated on Section 1 at a distance of d=65 km from terminal T1. The fault and ground resistances are set to $R_f = 1\ \Omega$ and $R_g = 0.1\ \Omega$, respectively. The total simulation duration is 1 s, with the fault occurring at t=0.65 s. The voltage waveforms at the three network terminals are shown in Fig. 5, while Fig. 6 illustrates the corresponding 1-mode voltage components for these terminals.

To detect the fault and identify the faulted section, the instantaneous frequency spectra of the three 1-mode voltage components are plotted in Fig. 7. Based on the proposed model in Section 2.7, the threshold value is determined as 0.9914. As observed, only the IFSPV corresponding to Section 1 exceeds this threshold, whereas the IFSPVs for the other two sections remain below it. This confirms successful fault detection and correctly identifies Section 1 as the faulted section.

In the next step, to classify the fault type, the IF components corresponding to the positive and negative pole voltages measured at terminal 1 are shown in Fig. 8. It is evident that the IFSPVs of the positive and negative poles differ significantly. In other words, the condition $E_{pn} < \varepsilon$ is not satisfied, confirming a pole-to-ground fault. To identify the faulted pole, the IFSPVs of the two poles are compared. Since the IFSPV of the positive pole voltage is higher, the fault is classified as a PTG fault.

In the final step, to estimate the fault location, the instantaneous frequency spectra corresponding to the positive pole voltage at terminal 1 and point M are plotted in Fig. 9, and the time instances associated with the IFSPVs in both spectra are identified. Then, based on the Eq. (14), the fault location is estimated as follows ($v = \frac{1}{\sqrt{LC}} = 2.582 \times 10^4 \frac{m}{s}$):

$$\hat{d} = \frac{v\left[t\left(IFSPV_{V_{P_k}}\right) - t\left(IFSPV_{V_{P_{k-1}}}\right)\right] + l}{2} = \frac{2.582\times10^4\,(0.6524-0.6512)+100}{2} = 65.4919 \text{ km} \tag{20}$$

While d=65 km and $\hat{d}$=65.4919 km, the relative estimation error is 0.4919%, and the accuracy of fault location estimation is 99.5081%.

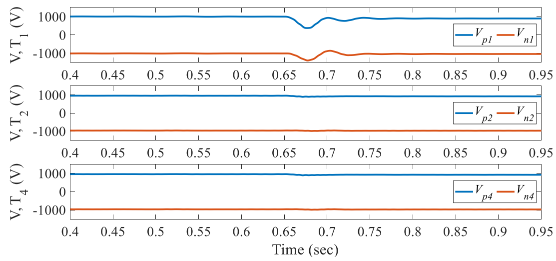

Fig. 5. Measured voltage waveforms at the three terminals of the multi-terminal HVDC system under Scenario 1, showing the initial transient response following fault occurrence.

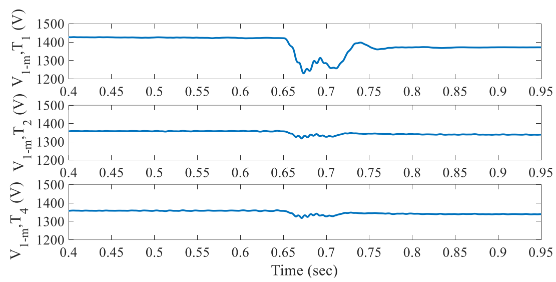

Fig. 6. Extracted 1-mode voltage components at the three terminals for Scenario 1, obtained using the Karrenbauer transform to reduce pole-coupling effects.

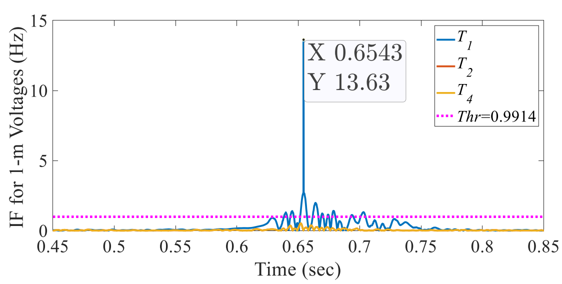

Fig. 7. Instantaneous frequency spectra of the 1-mode voltage components for Scenario 1, computed using the proposed modified frequency spectrum Hilbert transform (MFSHT), highlighting fault-induced frequency peaks used for detection and section identification.

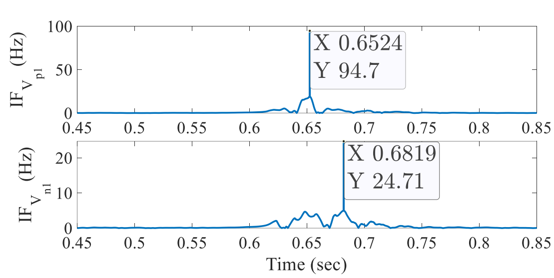

Fig. 8. Instantaneous frequency components of the positive and negative pole voltages measured at terminal 1 under Scenario 1, illustrating the differential response used for fault classification.

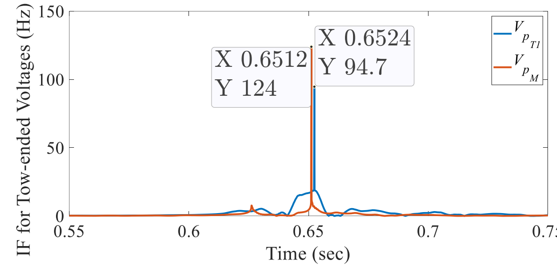

Fig. 9. Instantaneous frequency spectra of the positive pole voltage at terminal 1 and measurement point M for Scenario 1, highlighting the peak frequency features utilized in fault detection and location estimation.

3.2. NTG fault scenario on Section 2 at a distance of d=22 km

In this scenario, while maintaining the same fault parameters as in the previous case, an NTG fault occurs on Section 2 at a distance of d=22 km from the measurement point (T_2). The results for this scenario are presented in Figs. 10 to 12. Fig. 10 confirms the detection of the fault and the identification of section 2 as the faulted section. Additionally, in Fig. 11, a significant difference between IFSPVs corresponding to V_{P_2} and V_{N_2} is observed. Since $IFSPV_{V_{P_2}} < IFSPV_{V_{N_2}}$, the fault is classified as an NTG fault.

The time instances corresponding to the detected IFSPV values in the instantaneous frequency spectra associated with V_{N_2} and V_{Nm} in Fig. 12 are 0.6542s and 0.6564s, respectively. Using the following equation, the estimated fault location is determined as d=21.5981 km.

$$\hat{d} = \frac{v\left[t\left(IFSPV_{V_{N_k}}\right)-t\left(IFSPV_{V_{N_{k-1}}}\right)\right]+l}{2} = \frac{2.582\times10^4\,(0.6542-0.6564)+100}{2} = 21.5981 \text{ km} \tag{21}$$

Given that d=22 km and the estimated fault location is $\hat{d}$=21.5981 km, the relative estimation error is 0.4019%, and the accuracy of the estimation is 99.5981%.

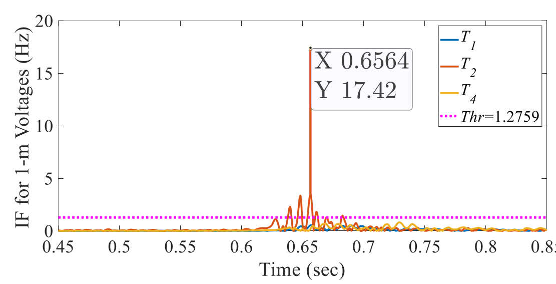

Fig. 10. Instantaneous frequency spectra of the three 1-mode voltage components under Scenario 2, obtained using the proposed MFSHT, highlighting fault-induced frequency variations at each terminal.

3.3. PTN fault scenario on Section 3 at a distance of d=87 km

In the third scenario, a pole-to-pole (PTN) fault occurs on the third section of the simulated system at a distance of d=87 km from the measurement point (T_3). It should be noted that the fault parameters remain unchanged. The graphical results are presented in Figs. 13 to 15. Fig. 13 confirms the occurrence of the fault on the third section. Additionally, in Fig. 14, the E_{pn} parameter is 0.26 Hz, which is less than the threshold value of ε =1 Hz (see Table 2). As a result, the PTN fault type is identified. Given that the fault type is PTN, the Eq. (16) should be applied to estimate the fault location based on the time components presented in Fig. 15, as follows:

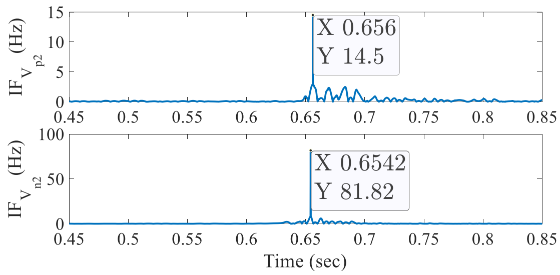

Fig. 11. Instantaneous frequency components of the positive and negative pole voltages measured at terminal 2 under Scenario 2, showing differential behavior used for fault type classification.

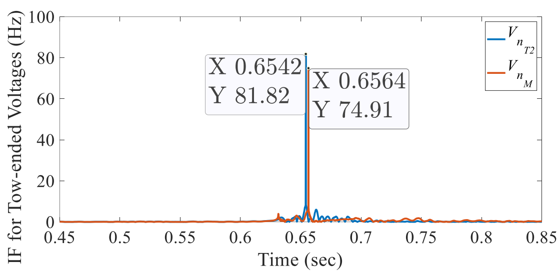

Fig. 12. Instantaneous frequency spectra of the negative pole voltage at terminal 2 and measurement point M for Scenario 2, emphasizing peak frequency features utilized in fault detection and fault location estimation.

$$\begin{cases} \Delta t_p = t\left(IFSPV_{V_{P_k}}\right) - t\left(ISPV_{V_{P_{k-1}}}\right) = \\ \quad 0.6561 - 0.6523 = 0.0038 \text{ s} \\ \Delta t_n = t\left(ISPV_{V_{N_k}}\right) - t\left(ISPV_{V_{N_{k-1}}}\right) = \\ \quad 0.6553 - 0.6534 = 0.0019 \text{ s} \end{cases} \tag{22}$$

$$\Delta t_{\text{actual}} = \frac{0.0038 + 0.0019}{2} = 0.0029 \text{ s} \tag{23}$$

$$\hat{d} = \frac{v\Delta t_{\text{actual}} + l}{2} = \frac{2.582\times10^4\times0.0029+100}{2} = 87.439 \text{ km} \tag{24}$$

With d=87 km and the estimated fault location $\hat{d}$=87.439 km, the relative estimation error is 0.4390%, and the accuracy of the estimation is 99.5610%.

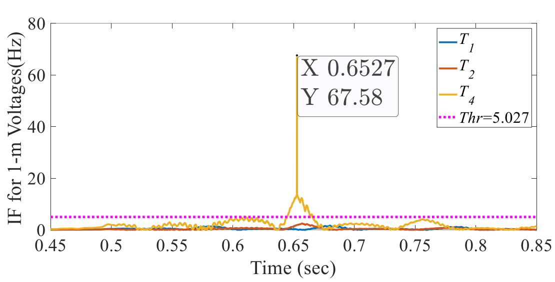

Fig. 13. Instantaneous frequency spectra of the three 1-mode voltage components under Scenario 3, obtained using the proposed MFSHT, highlighting fault-induced frequency variations across all terminals.

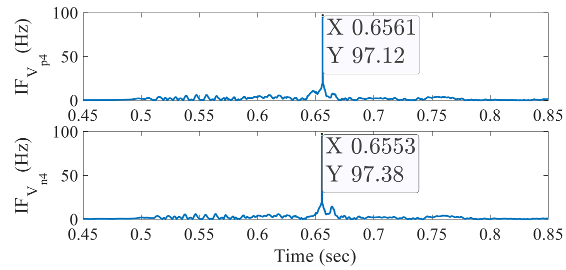

Fig. 14. Instantaneous frequency components of the positive and negative pole voltages measured at terminal 4 under Scenario 3, showing differential characteristics used for fault classification.

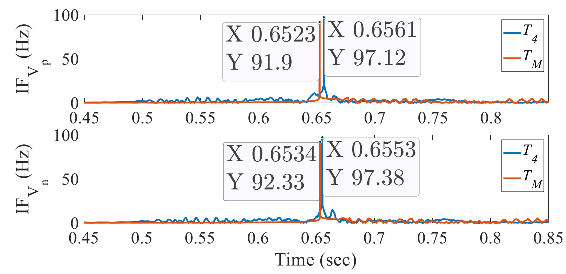

Fig. 15. Instantaneous frequency spectra of the positive and negative pole voltages at terminal 4 and measurement point M for Scenario 3, illustrating peak frequency features applied in fault detection and fault location estimation.

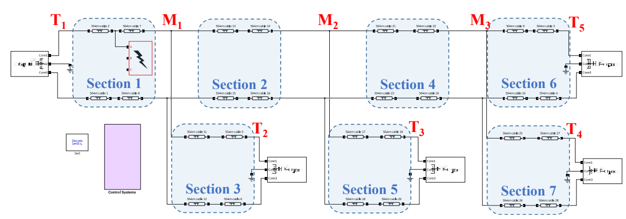

Fig. 16. Simulated five-terminal HVDC system.

4. SCALABILITY ASSESSMENT OF THE PROPOSED METHOD

To further demonstrate the scalability and general applicability of the proposed protection scheme, additional simulations were carried out on a larger multi-terminal HVDC (MTDC) network. While the previous case studies were based on a three-terminal configuration, this section extends the validation to an MTDC system with N=5 terminals in order to evaluate the impact of network size on the detection accuracy, fault location performance, and computational burden of the method. The considered extended network preserves the same control and operating principles as the baseline system but incorporates additional terminals and interconnections, thereby representing a more realistic scenario for practical HVDC grids. The simulated system is depicted in Fig. 16.

Owing to space constraints, this paper presents only the results for the analysis of the eight 1-mode voltage components measured at the eight designated measurement points. These components are processed by the proposed method for the purposes of fault detection and faulty-section identification. Once the faulty section is identified, the subsequent steps—namely fault type determination and fault location estimation—are carried out in the same manner as in the three-terminal system. This procedure is essentially independent of the total number of terminals, as it relies solely on the positive- and negative-pole voltage signals of the section in which the fault occurs. Therefore, the main distinction in larger systems lies in the initial signal processing stage required for detecting and locating the faulty section, while the following fault analysis stages remain unchanged.

Table 3 summarizes the results for several fault scenarios occurring at different distances and sections within the five-terminal system. Additionally, the graphical results corresponding to Fault Scenario 2 are depicted in Figs. 17-19. These figures illustrate the extracted 1-mode voltage components, their instantaneous frequency spectra, and the corresponding fault indicators, demonstrating the effectiveness of the proposed method in accurately identifying the faulty section and estimating the fault characteristics. Overall, the results confirm that the methodology maintains high accuracy and robustness, even as the system complexity increases from three to five terminals.

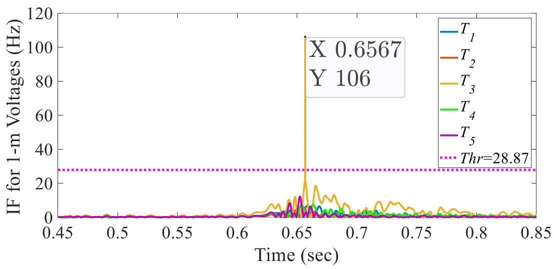

Fig. 17. Instantaneous frequency spectra of the five 1-mode voltage components under Scenario 2 in Table 3, obtained using the proposed MFSHT, highlighting fault-induced frequency variations across all terminals.

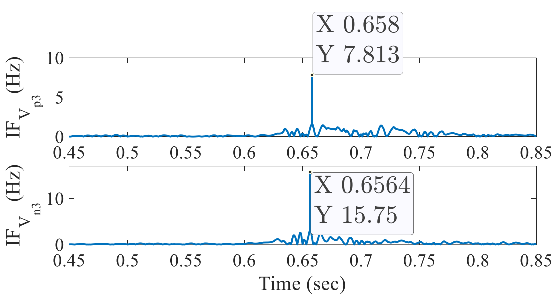

Fig. 18. Instantaneous frequency components of the positive and negative pole voltages measured at terminal 3 under Scenario 2 in Table 3, showing differential characteristics used for fault classification.

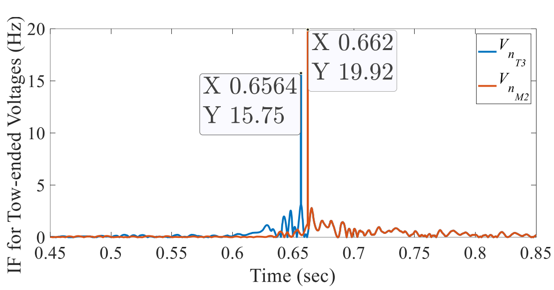

Fig. 19. Instantaneous frequency spectra of the negative pole voltages at terminal 3 and measurement point M_2 for Scenario 2 in Table 3, illustrating peak frequency features applied in fault detection and fault location estimation.

Fig. 17 illustrates that the IF of the voltage measured at Terminal 3 exceeds the predefined threshold, thereby indicating that the section connected to this terminal is the faulted section. Figs. 18 and 19, analogous to the previous three-terminal scenarios, identify the negative pole as the faulted pole (NTG fault) and estimate the fault location at 72.9611 km.

5. SENSITIVITY ANALYSIS

In this section, sensitivity analyses are performed to assess the robustness of the proposed protection algorithm under dynamic operating conditions. The analysis covers a wide range of scenarios, including variations in fault resistance, fault location, faulted section, and fault type, as well as the presence of noise in measured voltage signals, changes in line length, measurement synchronization errors, and nonlinear high-impedance arcing faults. The following subsections present the results for each case.

5.1. Impact of fault resistance on protection algorithm performance

To evaluate the performance of the proposed protection scheme in fault detection, classification, section identification, and location estimation, simulations are conducted for different values of fault resistance, specifically R_f=1,10,50,100,200Ω. The results are presented in Table 4. It should be noted that the actual fault location in all scenarios is d=40 km, and the fault type is assumed to be a PTG fault on section 1 with a ground resistance of R_g=0.1Ω.

The results presented in Table 4 indicate that increasing fault resistance significantly impacts the magnitude of the IFSPV components. However, the performance of fault detection, classification, and section identification remains unaffected, achieving 100% accuracy in all scenarios. On the other hand, while the time components corresponding to IFSPV are not significantly influenced by increasing fault resistance, the sensitivity of the fault location estimation algorithm to these time components leads to a rise in estimation error. Specifically, the results demonstrate that as the fault impedance increases from 1Ω to 200Ω, the estimation error increases by 79.46%.

5.2. Impact of fault location on protection algorithm performance

To evaluate the performance of the proposed protection algorithm under varying fault locations, simulations were conducted for different fault distances from terminal T_1 on Section 1, with a default fault resistance of R_f=1Ω. The results are presented in Table 5. It should be noted that the fault type is assumed to be PTG in all cases.

The results presented in Table 5 demonstrate the high accuracy of the proposed model in fault location estimation. It is evident that for all simulated fault distances, the model achieves 100% accuracy in fault detection, classification, and section identification. Additionally, the average error in fault location estimation is 0.0832%. These findings confirm the robustness and reliability of the proposed model under varying fault location conditions.

5.3. Impact of fault type and faulted section on protection algorithm performance

To assess the performance of the proposed protection scheme under different fault scenarios across various sections, three fault types—PTG, NTG, and PTN—are simulated on Sections 1, 2, and 3 under identical conditions. The fault distance for all cases is assumed to be d=65 km from the measurement point, with fault and ground resistances set at R_f=1Ω and R_g=0.1Ω, respectively. The results are presented in Table 6 (t_f=0.65s).

The numerical results presented in Table 6 confirm the high accuracy of the proposed protection model in fault detection, fault section determination, fault phase identification, and fault location estimation across all fault scenarios. These findings demonstrate that variations in fault type and fault section do not significantly impact the accuracy of the proposed model. Notably, the standard deviation of the estimation errors is 0.0471 (less than 1%), highlighting the robustness and reliability of the fault location model against changes in fault characteristics.

Table 3. Summary of fault detection, faulty-section identification, and fault location estimation results for various fault scenarios at different distances and sections in the five-terminal system ($R_f = 1\,\Omega$, $R_g = 0.1\,\Omega$).

Fault scenario	$\mathbf{IFSPV}_{V_{(1\text{-}mode)_1}}$ $\mathbf{IFSPV}_{V_{(1\text{-}mode)_2}}$ $\mathbf{IFSPV}_{V_{(1\text{-}mode)_3}}$ $\mathbf{IFSPV}_{V_{(1\text{-}mode)_4}}$ $\mathbf{IFSPV}_{V_{(1\text{-}mode)_5}}$		$\mathbf{Thr}_{IF_{(k,i)}}$	$\mathbf{IFSPV}_{V_{P_j}}$ **j=Number of foulted section (1,2,3,4,5)**		$\mathbf{IFSPV}_{V_{n_j}}$ **j=Number of foulted section (1,2,3,4,5)**	$t(\mathbf{IFSPV}_{V_{P_k}})$ $t(\mathbf{IFSPV}_{V_{P_M}})$ $t(\mathbf{IFSPV}_{V_{n_k}})$ $t(\mathbf{IFSPV}_{V_{n_m}})$ $k = 1, 2, 3, 4, 5$ $M = 1, 2, 3$	$\hat{d}$	**Estimation error (%)**
PTG on Section 1 at a distance of 38 km	104.22 13.74 13.55 12.96 12.35	$>$ $<$ $<$ $<$ $<$	27.48	53.69	$>$	27.25	0.6510287 0.6539551	38.0530	0.0530
NTG on Section 3 at a distance of 73 km	14.11 13.97 106.03 13.03 13.54	$<$ $<$ $>$ $<$ $<$	27.87	23.10	$<$	38.21	0.6564179 0.6620422	72.9611	0.0389
PTN on Section 6 at a distance of 89 km	12.56 10.24 10.73 11.42 108.94	$<$ $<$ $<$ $<$ $>$	27.32	25.36	$\approx$	25.41	0.6538541 0.6442836 0.6545405 0.6449935	89.0234	0.0234
Mean value									0.0543
Standard deviation									0.0257

Table 4. Numerical results corresponding to the sensitivity analysis of the fault resistance.

Fault resistance Ω	$\mathbf{IFSPV}_{V_{(1\text{-}mode)_1}}$ $\mathbf{IFSPV}_{V_{(1\text{-}mode)_2}}$ $\mathbf{IFSPV}_{V_{(1\text{-}mode)_3}}$		$\mathbf{Thr}_{IF_{(k,i)}}$	$\mathbf{IFSPV}_{V_{P_1}}$		$\mathbf{IFSPV}_{V_{n_1}}$	$t(\mathbf{IFSPV}_{V_{P_1}})$ $t(\mathbf{IFSPV}_{V_{P_M}})$	$\hat{d}$	**Estimation error (%)**
1	14.73 0.3754 0.3754	$>$ $<$ $<$	1.0784	110.1	$>$	24.89	0.6512582 0.6520247	40.1035	0.1035
50	5.244 0.2536 0.2536	$>$ $<$ $<$	0.3780	24.75	$>$	2.478	0.65133479 0.65214058	39.5973	0.4027
200	0.3719 0.08393 0.08393	$>$ $<$ $<$	0.2368	6.18	$>$	0.947	0.65135890 0.65217253	39.4961	0.5039
Mean value									0.3461
Standard deviation									0.1702

5.4. Impact of line length on protection algorithm performance

To assess the robustness of the proposed protection algorithm across different system configurations, a sensitivity analysis was conducted with transmission lines of varying lengths. This subsection examines the impact of line length on the accuracy of fault detection, classification, and location. Specifically, a PTG fault was simulated at a distance of d=85 km from the measurement point on Section 1 using predefined fault parameters. Line lengths were considered in three scenarios: 100 km, 200 km, and 300 km per section. The results corresponding to these configurations are summarized in Table 7.

The results in Table 7 demonstrate that line length has a tangible impact on the numerical values of the IFSPV indices. Despite these variations, the proposed algorithm successfully discriminates between fault and non-fault cases, as indicated by the threshold comparison results remaining consistent across all scenarios. Moreover, the fault location estimates remain highly accurate. The estimated distances ($\hat{d}$) are closely aligned with the actual fault location (85 km), with errors remaining below 0.15% for all line lengths.

Overall, the sensitivity analysis confirms that the proposed method is robust against changes in line length. Although the signal magnitudes and time indices slightly vary with increasing distance, the detection, classification, and localization functions maintain high accuracy and reliability. This validates the algorithm's suitability for application in practical transmission systems of different scales.

5.5. Impact of measurement noise on protection algorithm performance

In this subsection, measurement noise is introduced into the voltage signals recorded at the network terminals. This noise can originate from various sources, including electromagnetic interference, grounding and common-mode noise, capacitive coupling, or harmonics from converters. To analyze the impact of measurement noise, five different SNR values are simulated for the measured voltages, with the results presented in Table 8. It should be noted that the fault type in all cases is assumed to be a PTG fault occurring on Section 1 at a distance of d=32 km. The fault and ground resistance parameters are set to R_f=1Ω and R_g=0.1Ω, respectively.

Additionally, as an illustrative example, graphical results for the worst-case scenario, where SNR=20 dB, are depicted in Figs. 20 to 22. The results in Table 8 and Figs. 20 to 22 confirm the accurate performance of the proposed model in fault section detection,

Table 5. Optimal DGs power generations by Jaya algorithm under various fault conditions.

Fault resistance Ω	$\mathbf{IFSPV}_{V_{(1\text{-}mode)_1}}$ $\mathbf{IFSPV}_{V_{(1\text{-}mode)_2}}$ $\mathbf{IFSPV}_{V_{(1\text{-}mode)_3}}$		$\mathbf{Thr}_{IF_{(k,i)}}$	$\mathbf{IFSPV}_{V_{P_1}}$		$\mathbf{IFSPV}_{V_{n_1}}$	$t(\mathbf{IFSPV}_{V_{P_1}})$ $t(\mathbf{IFSPV}_{V_{P_M}})$	$\hat{d}$	**Estimation error (%)**
5	14.56 0.3375 0.3375	> < <	1.0737	102.5	>	24.32	0.65034561 0.65382296	5.1076	0.1076
50	15.45 0.4305 0.4305	> < <	1.1317	101.1	>	24.98	0.6515972 0.6516120	49.8087	0.1913
95	9.993 0.6331 0.6331	> < <	0.7091	70.32	>	27.99	0.6538125 0.6503252	95.0216	0.0216
Mean value									0.0832
Standard deviation									0.0478

Table 6. Numerical results corresponding to the sensitivity analysis of the fault type and faulted section.

Faulty Section	**Fault type**	$\mathbf{IFSPV}_{V_{(1\text{-}mode)_1}}$ $\mathbf{IFSPV}_{V_{(1\text{-}mode)_2}}$ $\mathbf{IFSPV}_{V_{(1\text{-}mode)_3}}$		$\mathbf{Thr}_{IF_{(k,i)}}$	$\mathbf{IFSPV}_{V_{P_1}}$ $\mathbf{IFSPV}_{V_{P_2}}$ $\mathbf{IFSPV}_{V_{P_3}}$		$\mathbf{IFSPV}_{V_{n_1}}$ $\mathbf{IFSPV}_{V_{n_2}}$ $\mathbf{IFSPV}_{V_{n_3}}$	$t(\mathbf{IFSPV}_{V_{P_k}})$ $t(\mathbf{IFSPV}_{V_{P_M}})$ $t(\mathbf{IFSPV}_{V_{n_k}})$ $t(\mathbf{IFSPV}_{V_{n_M}})$ $\boldsymbol{k=1,2,3}$	$\hat{d}$	**Estimation error (%)**
1	PTG	13.68 0.4608 0.4608	> < <	0.9944	95.1 NM* NM	>	24.91 NM NM	0.6522896 0.6511158 NM NM	65.1537	0.1537
2	NTG	0.6505 11.41 0.6505	< > <	0.8029	NM 1.055 NM	$\lessapprox$	NM 22.2 NM	NM NM 0.6522453 0.6510753	65.1054	0.1054
3	PTN	0.945 0.945 57.82	< < >	4.1424	NM NM 93.03	$\approx$	NM NM 93.48	0.6522433 0.6510586 0.6523152 0.6511684	65.0497	0.0497
Mean value										0.1101
Standard deviation										0.0471
* NM: Not measured										

classification, and identification. Moreover, it is observed that for lower SNR values, the error in fault location estimation increases slightly, whereas the error in fault detection, classification, and section determination remains zero. The standard deviation of the estimation error is calculated as 0.1753, while the average estimation error is 0.1955, both of which are significantly less than 1%. These findings indicate that reducing the SNR from 60 dB to 20 dB results in a 97.38% increase in the estimation error. However, the highest estimation error percentage is observed in the R_f=200Ω scenario, suggesting that the impact of increasing fault resistance on the accuracy of the fault location estimation model is greater than that of measurement noise.

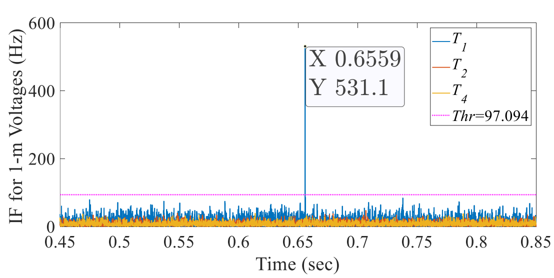

Fig. 20. The instantaneous frequency (IF) spectra of the three 1-mode voltage components under noisy conditions with SNR=20 dB.

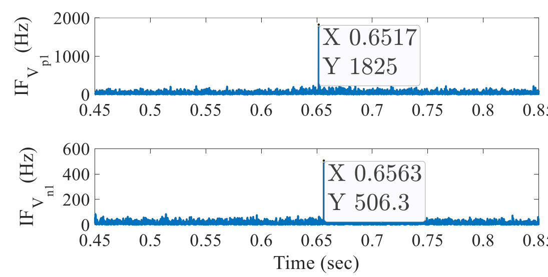

Fig. 21. The IF components corresponding to the positive and negative pole voltages measured at terminal 1 under noisy conditions with SNR=20 dB.

5.6. Impact of measurement synchronization errors on algorithm performance

To evaluate the robustness of the proposed protection algorithm under realistic conditions, a sensitivity analysis was carried out considering possible measurement synchronization errors. Since the proposed scheme relies on traveling-wave features extracted from terminal voltage signals, synchronization accuracy between measurement units can directly influence the reliability of fault detection and location.

In this study, synchronization errors were emulated by artificially shifting the recorded voltage signals with respect to each other by predefined time offsets. Three representative scenarios were

Table 7. Numerical results corresponding to the sensitivity analysis of the line length.

Line length (km)	$\mathbf{IFSPV}_{V_{(1\text{-}mode)_1}}$ $\mathbf{IFSPV}_{V_{(1\text{-}mode)_2}}$ $\mathbf{IFSPV}_{V_{(1\text{-}mode)_3}}$		$\mathbf{Thr}_{IF_{(k,i)}}$	$\mathbf{IFSPV}_{V_{P_1}}$		$\mathbf{IFSPV}_{V_{n_1}}$	$t(\mathbf{IFSPV}_{V_{P_1}})$ $t(\mathbf{IFSPV}_{V_{P_M}})$	$\hat{d}$	**Estimation error (%)**
100	12.45 0.3132 0.3345	> < <	0.9984	98.63	>	15.3	0.6431086 0.6517036	85.0889	0.0889
200	10.732 0.2234 0.2155	> < <	0.8523	113.44	>	25.1	0.6651213 0.6723795	85.1843	0.0921
300	7.918 0.1586 0.1749	> < <	0.6658	148.98	>	36.42	0.6515663 0.6990223	85.4206	0.1402
Mean value									0.1071
Standard deviation									0.0287

Table 8. Numerical results corresponding to the sensitivity analysis of the measurement noise.

SNR (dB)	$\mathbf{IFSPV}_{V_{(1\text{-}mode)_1}}$ $\mathbf{IFSPV}_{V_{(1\text{-}mode)_2}}$ $\mathbf{IFSPV}_{V_{(1\text{-}mode)_3}}$		$\mathbf{Thr}_{IF_{(k,i)}}$	$\mathbf{IFSPV}_{V_{P_1}}$		$\mathbf{IFSPV}_{V_{n_1}}$	$t(\mathbf{IFSPV}_{V_{P_1}})$ $t(\mathbf{IFSPV}_{V_{P_M}})$	$\hat{d}$	**Estimation error (%)**
20	531.1 32.15 44.87	> < <	97.094	1825	>	506.3	0.6517825 0.6532123	31.5414	0.4586
40	158.2 8.562 14.61	> < <	26.279	397.6	>	116.1	0.6518276 0.6532359	31.8189	0.1811
60	28.78 2.084 1.897	> < <	4.7494	128.6	>	33.89	0.6518160 0.6532112	31.9880	0.0120
Mean value									0.1955
Standard deviation									0.1753

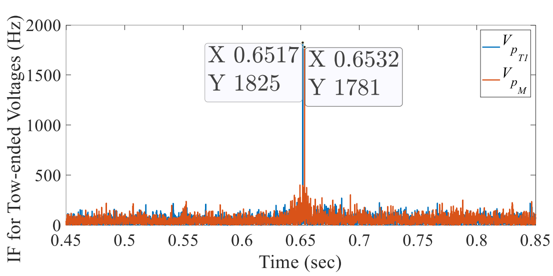

Fig. 22. The instantaneous frequency spectra corresponding to the positive pole voltage at terminal 1 and point M under noisy conditions with SNR=20 dB.

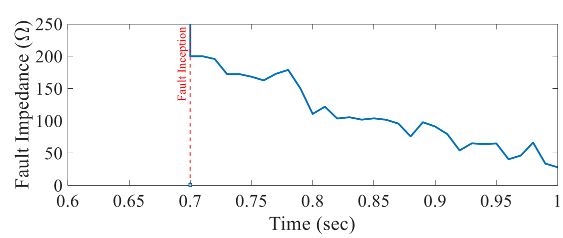

Fig. 23. Fault resistance under variable-impedance arcing conditions for the sensitivity analysis scenario (subsection 5.7).

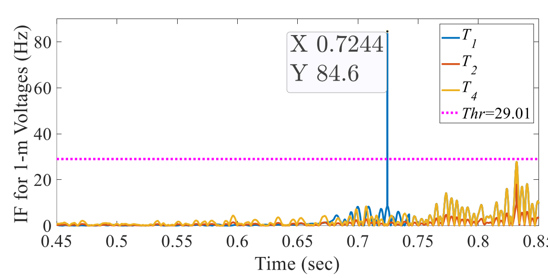

Fig. 24. The instantaneous frequency (IF) spectra of the three 1-mode voltage components under nonlinear high-impedance arcing conditions.

considered, namely 1 μs, 5 μs, and 10 μs synchronization errors, which correspond to typical tolerances of GPS- and PMU-based measurement systems in practical HVDC grids. The results are presented in Table 9. It should be noted that, for this case, a PTG fault was simulated on Section 1 using the parameters specified in subsection 5.2, with the actual fault located at a distance of d=62 km.

The results in Table 9 demonstrate that although synchronization errors introduce noticeable variations in the secondary modal components, the primary modal signal used in the proposed scheme remains stable. The detection thresholds exhibit only minor fluctuations, ensuring reliable discrimination between fault and non-fault conditions. In terms of fault location, the estimation error increases slightly with larger synchronization offsets, from approximately 0.05 km at 1 μs to about 0.7 km at 10 μs. This error corresponds to less than 1% of the line length, which is well within acceptable margins for practical HVDC protection applications. The mean and standard deviation values further confirm that the proposed algorithm maintains stable and accurate performance under realistic synchronization tolerances,

Table 9. Numerical results corresponding to the sensitivity analysis of the synchronization error.

Δt_{sync} (μs)	$\mathbf{IFSPV}_{V_{(1\text{-}mode)_1}}$ $\mathbf{IFSPV}_{V_{(1\text{-}mode)_2}}$ $\mathbf{IFSPV}_{V_{(1\text{-}mode)_3}}$		$\mathbf{Thr}_{IF_{(k,i)}}$	$\mathbf{IFSPV}_{V_{P_1}}$		$\mathbf{IFSPV}_{V_{n_1}}$	$t(\mathbf{IFSPV}_{V_{P_1}})$ $t(\mathbf{IFSPV}_{V_{P_M}})$	$\hat{d}$	**Estimation error (%)**
1	55.26 14.02 5.124	> < <	18.0575	95.79	>	23.66	0.6530526 0.6501247	61.9531	0.0469
5	55.38 15.15 6.023	> < <	19.1456	96.33	>	24.78	0.6545561 0.6515463	62.2875	0.2875
10	57.42 17.88 8.167	> < <	19.6674	102.24	>	31.58	0.6555682 0.6524564	62.7039	0.7039
Mean value									0.3461
Standard deviation									0.2733

Table 10. Numerical results corresponding to the sensitivity analysis of the nonlinear high-impedance arcing.

Fault scenario	$\mathbf{IFSPV}_{V_{(1\text{-}mode)_1}}$ $\mathbf{IFSPV}_{V_{(1\text{-}mode)_2}}$ $\mathbf{IFSPV}_{V_{(1\text{-}mode)_3}}$		$\mathbf{Thr}_{IF_{(k,i)}}$	$\mathbf{IFSPV}_{V_{P_1}}$		$\mathbf{IFSPV}_{V_{n_1}}$	$t(\mathbf{IFSPV}_{V_{P_1}})$ $t(\mathbf{IFSPV}_{V_{P_M}})$	$\hat{d}$	**Estimation error (%)**
A PTG fault on Section 1 at a distance of 9 km under nonlinear high-impedance arcing conditions	84.60 11.13 6.27	> < <	29.01	100.2	>	7.438	0.7027558 0.7128336	8.8572	0.1428

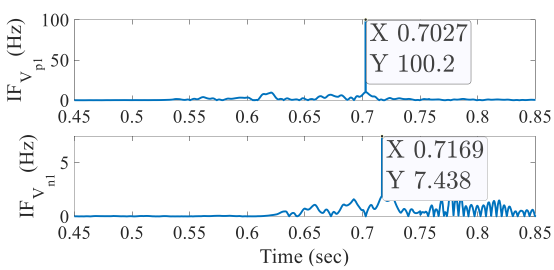

Fig. 25. The IF components corresponding to the positive and negative pole voltages measured at terminal 1 under nonlinear high-impedance arcing conditions.

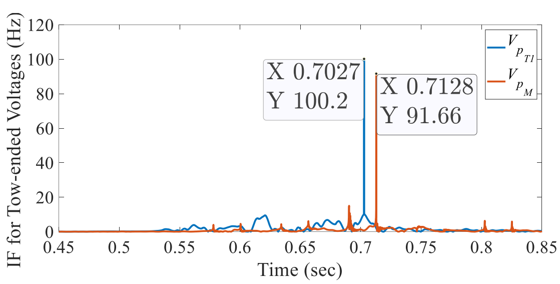

Fig. 26. The instantaneous frequency spectra corresponding to the positive pole voltage at terminal 1 and point M under nonlinear high-impedance arcing conditions.

highlighting its robustness against measurement synchronization errors.

5.7. Impact of nonlinear high-impedance arcing on algorithm performance

To further examine the robustness of the proposed protection scheme under more realistic high-impedance fault (HIF) conditions, an arcing ground fault was simulated with a time-varying fault resistance. Unlike the fixed-resistance scenario discussed in Section 5.1, here the fault resistance decreases from an initial value of 200 Ω toward a lower bound of 20 Ω, while superimposed Gaussian fluctuations emulate the random and nonlinear behavior typically observed in arcing HIFs. The simulated fault was a pole-to-ground (PTG) fault on Section 1 at a distance of 9 km from the measurement point, occurring at t = 0.7 s. Fig. 23 depicts the resistance variation profile, which remains infinite before the inception of the fault and then exhibits both a downward trend and stochastic oscillations. Figs. 24-26 illustrate the subsequent outputs of the proposed method, corresponding respectively to section identification, fault-type determination, and fault-location estimation. These results demonstrate that the algorithm maintains accurate and reliable performance even under nonlinear arcing HIF conditions, thereby confirming its robustness beyond the fixed-resistance cases.

Furthermore, the information extracted from the graphical outputs is listed numerically in Table 10. As observed, the proposed scheme maintains accurate fault detection and classification even under nonlinear high-impedance arcing conditions. However, the time-domain components derived from the instantaneous frequency corresponding to the voltages at both ends of the faulted section exhibit slightly reduced precision, which leads to a larger error in the estimated fault location. This behavior can be attributed to the stochastic fluctuations of the fault resistance during arcing, which introduce small variations in the voltage waveforms and slightly affect the phase and timing information used for location estimation.

6. COMPARATIVE STUDY

To verify the performance of the proposed protection scheme, this section presents a comparative analysis with existing methods reported in the literature. Since comparing the response speed of different protection schemes requires a consistent computational environment, the numerical results provided in this section are based on simulations conducted on a computer equipped with an Intel Core i7 processor (2.7 GHz) and 8 GB RAM. Furthermore, all simulations were performed in the MATLAB R2021b environment. The results of this comparative analysis are summarized in Table 11.

Table 11. Results of comparative study against the existing methods.

Ref./Info.	[24]	[25]	[26]	[27]	[28]	[29]	[30]	[31]	[32]	**This work**
Utilized method	DC Reactor Voltage Change Rate	Wavelet Transform, Fuzzy C-Means Classification, Neural Networks	Rate-of-Change-of-Current and Rate-of-Change-of-Voltage	Stationary Wavelet Transform and Singular Value Decomposition	Machine Learning-Based Algorithm	Control and Protection Coordination Strategy	Fuzzy Inference System	Kalman Filter and Least Squares (LS) Algorithm	Extreme Gradient Boosting (AI Technique)	Troweling Wave Based Modified Frequency-Spectrum Hilbert Transform
Measured signal	Voltage across the DC terminal reactor	Current signals	Voltage and current signals	Current signals	Voltage signal	Current signals	Current signals	Voltage and current signals	Local current and voltage signals	Voltage signals
Fault detection capability	✓	✓	✓	✓	✓	✓	✓	✓	✓	✓
Fault classification capability	×	✓	✓	✓	×	✓	✓	✓	✓	✓
Faulty segment determination capability	✓	✓	NR	✓	×	✓	✓	✓	✓	✓
Fault locating estimation capability	✓	✓	×	✓	✓	✓	×	✓	×	✓
Fault detection accuracy	NR	NR	NR	NR	NR	NR	100%	NR	98%	100%
Fault classification accuracy	NR	NR	NR	NR	–	NR	NR	NR	NR	100%
Faulty section determination accuracy	NR	NR	NR	NR	–	NR	NR	NR	NR	100%
Fault location accuracy	NR	NR	–	As small as 0.5 km	NR	NR	–	99%	–	Averaged 99.8168%
Sensitivity analysis to the fault resistance	✓	✓	✓	✓	✓	✓	✓	✓	✓	✓
Sensitivity analysis to the fault type	✓	✓	✓	✓	✓	✓	✓	✓	✓	✓
Sensitivity analysis to the fault location	×	✓	✓	✓	✓	✓	✓	✓	✓	✓
Sensitivity analysis to the noisy conditions	✓	✓	×	✓	✓	✓	NR	✓	✓	✓
Average fault location error	NR	0.002%	–	0.007% of 100 km	0.516%	0.2%	–	0.54%	–	0.1837%
Maximum fault location error	NR	0.0013%	–	–	0.624%	0.45%	–	1.26%	–	0.5039%
Standard deviation of the fault location error	NR	NR	–	–	–	–	–	–	–	0.0627
Computational burden	Low to medium	High	Medium to high	Moderate to high	Low to medium	Medium	Relatively low	Relatively low	Low	Low
Time elapsed for fault detection	Less than 1.4–1.8 ms	0.38 ms	0.095–1.250 ms	Less than 1 ms	2.5 ms	150 ms	4–5 ms	Within 1 ms	Less than 2 ms	Averaged 0.35 ms
Time elapsed for fault classification	Less than 1.4–1.8 ms	NR	5 μs–10 μs	Less than 1 ms	–	150 ms	4–5 ms	Within 1 ms	Within 2 ms	Averaged 0.7 ms
Time elapsed for fault location	Less than 1.4–1.8 ms	NR	–	Within 1 ms	2.5 ms	150 ms	–	Less than 1 ms	–	Averaged 0.92 ms
Utilized threshold value for fault detection	Fixed	Adaptive	Adaptive	Adaptive	Adaptive	Adaptive	Adaptive	Fixed	Adaptive	Adaptive

The results of the comparative study presented in Table 11 highlight the superior performance of the proposed MFSHT-based protection model compared with existing methods in the literature. While some studies on MTHVDC protection address only fault detection and location [24], [28], the ability of the proposed model to simultaneously perform detection, classification, and section identification within a unified framework represents a significant advancement. Although certain learning-based methods, such as neural networks [25] or singular value decomposition approaches [27], achieve high accuracy in fault location estimation, their practical deployment is constrained by high computational complexity and the requirement for prior fault data to train the algorithms. Moreover, these approaches typically rely on current measurements, which introduce additional challenges in HVDC systems.

In contrast, voltage-based measurement offers several practical benefits. Voltage signals can be acquired using capacitive dividers or optical sensors, ensuring galvanic isolation and enhanced safety. By comparison, current measurement requires high-power current transformers or Hall-effect sensors, which may introduce insulation difficulties and safety concerns. Voltage measurement techniques, such as resistive or capacitive dividers, also provide higher accuracy and long-term stability, being less sensitive to core saturation, temperature fluctuations, and magnetization effects. Additionally, voltage measurement reduces power losses, simplifies insulation design, and facilitates digital integration, making it particularly suitable for HVDC applications.

In summary, the proposed model combines high accuracy with low computational burden. It achieves 100% accuracy in fault detection, classification, and section identification, regardless of fault type, location, or system parameters. Its reliance solely on voltage measurements enables practical implementation with minimal technical challenges. The introduction of an adaptive threshold mechanism based on fault characteristics further enhances robustness. Moreover, the model's efficient transient response and energy-conscious design make it a reliable and effective solution for MTHVDC system protection.

The simulation results further demonstrate the computational efficiency of the proposed algorithm. Unlike hybrid time–frequency or learning-based methods, the MFSHT algorithm primarily operates in the time domain with frequency-spectrum correction, significantly reducing processing time. For a three-terminal HVDC system, it achieves real-time performance on standard computational platforms. The algorithm structure allows straightforward extension to n-terminal HVDC networks without a proportional increase in complexity. Since it relies solely on local voltage measurements and avoids iterative multi-scale decompositions or offline training, the computational load grows linearly with the number of terminals, ensuring scalability. Sensitivity analyses confirm that even as the system size increases, the algorithm maintains high fault detection accuracy, reliable section identification, and precise fault location estimation, demonstrating its suitability for deployment in large and complex HVDC topologies.

7. DISCUSSION AND RESEARCH LIMITATIONS

The proposed MFSHT-based protection algorithm has demonstrated high accuracy and computational efficiency in multi-terminal HVDC systems. Simulation results confirm that the algorithm reliably performs fault detection, classification, section identification, and location estimation with minimal computational burden. Its reliance solely on voltage measurements and adaptive thresholding enhances both practicality and robustness in diverse fault scenarios.

However, this study has certain limitations. The proposed algorithm has been tested only on benchmark three- and four-terminal HVDC systems, which may not fully represent the complexity of large-scale, real-world multi-terminal grids. Additionally, no experimental validation or hardware-in-the-loop (HIL) testing has been performed, and practical issues such as measurement noise, communication delays, and sensor non-idealities have not been fully addressed.

Despite these limitations, the algorithm offers several practical implications for real-world HVDC operation. Voltage-based measurements simplify insulation design, improve safety, reduce power losses, and facilitate integration with digital control systems. The low computational burden and linear scalability of the algorithm make it suitable for larger networks where real-time fault protection is critical.

On the other hand, the proposed method requires high-speed communication of voltage measurements between terminals and interconnection nodes. Using typical fiber-optic links, the resulting communication delay is on the order of a few milliseconds, which is negligible compared to line propagation times. Timestamped data ensures accurate fault detection and localization despite this delay. Furthermore, the proposed method is applicable to both bipolar and unipolar HVDC systems. It only requires voltage measurements at terminals and interconnection nodes, with minor adjustments for different grounding arrangements.

For future work, the proposed model can be extended and enhanced in multiple directions. Hardware-in-the-loop testing and experimental validation on pilot-scale HVDC setups are essential to confirm real-time performance and robustness under practical conditions. Integration with hybrid HVAC-HVDC systems and the application of AI-based adaptive thresholding or hybrid signal processing techniques could further improve accuracy and resilience. Additionally, exploring scalability to very large n-terminal HVDC grids and incorporating communication constraints or cyber-physical considerations will increase its applicability in modern power systems.

8. CONCLUSION

In this paper, a simple, fast, and highly accurate protection scheme is proposed for fault detection, classification, section determination, and fault location estimation in multi-terminal high-voltage direct current (MTHVDC) systems. The proposed scheme requires only voltage measurements at the network terminals and interconnection nodes. It employs a time-domain signal processing technique—the Hilbert transform (HT)—combined with a frequency modification algorithm to extract the time–frequency characteristics necessary to achieve the four aforementioned protection objectives. The proposed scheme demonstrates 100% accuracy in fault detection, classification, and section determination, while its average fault location estimation accuracy reaches 99.8468%. Additionally, because the scheme relies on voltage rather than current measurements, it offers several practical advantages, including simpler installation and faster transient response. Furthermore, a novel adaptive algorithm is introduced for threshold calculation, which dynamically adjusts based on real-time fault characteristics, thereby overcoming the limitations of traditional fixed-threshold models. Sensitivity analyses confirm the robust performance of the proposed scheme under diverse operating conditions. The results indicate that the standard deviation of the fault location estimation error is only 0.0627% on average, which is far below the recommended 1% threshold. The proposed scheme offers several advantages: low computational burden, short execution time, scalability for n-terminal HVDC networks, and straightforward implementation using standard voltage measurement devices. Moreover, it does not require complex time–frequency signal processing, supports adaptive thresholding in real time, and remains insensitive to parameter variations and operating uncertainties.

In future work, the performance of the proposed scheme will be extended to multi-terminal HVAC transmission systems with meshed structures as well as hybrid multi-terminal HVAC–HVDC networks. Given the increased fault scenario complexity in three-phase HVAC grids and the greater number of network branches, the scheme's enhanced accuracy and speed in fault detection, classification, section identification, and location estimation will play a critical role in ensuring reliable protection.

FUNDING SOURCES

This research did not receive any specific grant from funding agencies in the public, commercial, or not-for-profit sectors.

DECLARATION OF INTERESTS

The authors declare that they have no competing interests.

DATA STATEMENT

Data sharing is not applicable to this article, as no datasets were generated or analyzed during the current study.

ACKNOWLEDGEMENT

The authors acknowledge the use of artificial intelligence tools (e.g., ChatGPT by OpenAI) for language editing and clarity improvement during the preparation of this manuscript. The authors are fully responsible for the scientific content, analysis, and conclusions.

REFERENCES

[1] M. Muniappan, "A comprehensive review of DC fault protection methods in HVDC transmission systems," *Prot. Control Mod. Power Syst.*, vol. 6, Jan. 2021.

[2] M. Radwan and S. Azad, "Protection of multi-terminal HVDC grids: A comprehensive review," *Energies*, vol. 15, p. 9552, Dec. 2022.

[3] M. Z. Yousaf, H. Liu, A. Raza, and A. Mustafa, "Deep learning-based robust DC fault protection scheme for meshed HVDC grids," *CSEE J. Power Energy Syst.*, Jan. 2023.

[4] E. Akbari and M. S. Shadlu, "Fault detection, classification, and location in VSC-HVDC systems using metaheuristic optimized ANFIS and Hilbert Huang transform method," in *Proc. Int. Conf. Prot. Autom. Power Syst.*, (Shahrood, Iran), pp. 1–7, Jan. 2024.

[5] S. H. A. Niaki, J. S. Farkhani, Z. Chen, B. Bak-Jensen, and S. Hu, "An intelligent method for fault location estimation in HVDC cable systems connected to offshore wind farms," *Wind*, vol. 3, pp. 361–374, Aug. 2023.

[6] M. Raheel and A. Raza, "A support vector machine learning-based protection technique for MT-HVDC systems," *Energies*, vol. 13, p. 6668, Dec. 2020.

[7] E. Akbari and M. S. Shadlu, "An intelligent ANFIS-Based fault detection, classification, and location model for VSC-HVDC systems based on hybrid PCA-DWT signal processing technique," *Comput. Electr. Eng.*, vol. 120, p. 109763, Oct. 2024.

[8] A. Pragati, M. Mishra, P. K. Rout, D. A. Gadanayak, S. Hasan, and B. R. Prusty, "A comprehensive survey of HVDC protection system: Fault analysis, methodology, issues, challenges, and future perspective," *Energies*, vol. 16, p. 4413, May 2023.

[9] J. Aparna *et al.*, "A very fast and easily implementable support vector machine based relay algorithm to classify the fault and non fault disturbance in VSC HVDC terminals," *Electr. Power Syst. Res.*, vol. 220, p. 109380, July 2023.

[10] F. Wilches-Bernal *et al.*, "A survey of traveling wave protection schemes in electric power systems," *IEEE Access*, vol. 9, pp. 72949–72969, Jan. 2021.

[11] M. J. B. B. Davi, M. Oleskovicz, and F. V. Lopes, "A review of signal processing for fault diagnosis in systems with inverter-based resources and an improved high-frequency component-based disturbance detector," *Electr. Power Syst. Res.*, vol. 236, p. 110938, Aug. 2024.

[12] A. Imani, Z. Moravej, and M. Pazoki, "A novel time-domain method for fault detection and classification in VSC-HVDC transmission lines," *Int. J. Electr. Power Energy Syst.*, vol. 140, p. 108056, Feb. 2022.

[13] K. Rana, N. Kishor, R. Negi, and M. Biswal, "Fault detection and VSC-HVDC network dynamics analysis for the faults in its host AC networks," *Appl. Sci.*, vol. 14, p. 2378, Mar. 2024.

[14] K. Jashandeep *et al.*, "Fault detection and protection strategy for multi-terminal HVDC grids using wavelet analysis," *Energies*, vol. 18, p. 1147, Feb. 2025.

[15] L. Yiqing *et al.*, "Single-pole fault protection for MMC-HVDC transmission line based on improved transient-extracting transform," *Int. Trans. Electr. Energy Syst.*, vol. 31, Dec. 2021.

[16] J. A. Torres, R. C. D. Santos, A. G. D. Freitas, and P. T. L. Asano, "MMC-Based VSC-HVDC link fault protection using short-time fourier transform," in *Proc. 15th IEEE Int. Conf. Ind. Appl.*, (São Bernardo do Campo, Brazil), pp. 1456–1462, Nov. 2023.

[17] M. Radwan and S. P. Azad, "An outlier-based single-ended protection scheme for multi-terminal MMC-HVDC grids based on hilbert-huang transform," *IEEE Trans. Power Del.*, vol. 39, pp. 3535–3546, Oct. 2024.

[18] A. Pragati, D. A. Gadanayak, and M. Mishra, "Fault detection and fault phase identification in a VSC-MT-HVDC link using stockwell transform and teager energy operator," *Electr. Power Syst. Res.*, vol. 236, p. 110937, Aug. 2024.

[19] M. Farshad and M. Karimi, "Intelligent protection of CSC-HVDC lines based on moving average and maximum coordinate difference criteria," *Electr. Power Syst. Res.*, vol. 199, p. 107439, July 2021.

[20] D. Gutierrez-Rojas, I. T. Christou, D. Dantas, A. Narayanan, P. H. J. Nardelli, and Y. Yang, "Performance evaluation of machine learning for fault selection in power transmission lines," *Knowl. Inf. Syst.*, vol. 64, pp. 859–883, Feb. 2022.

[21] W. Chen, D. Wang, D. Cheng, and X. Liu, "Travelling wave fault location approach for MMC-HVDC transmission line based on frequency modification algorithm," *Int. J. Electr. Power Energy Syst.*, vol. 143, p. 108507, Jul 2022.

[22] S. Gao, Z. Xu, G. Song, M. Shao, and Y. Jiang, "Fault location of hybrid three-terminal HVDC transmission line based on improved LMD," *Electr. Power Syst. Res.*, vol. 201, p. 107550, Sep 2021.

[23] L.-S. Law, J. H. Kim, W. Y. H. Liew, and S.-K. Lee, "An approach based on wavelet packet decomposition and Hilbert–Huang transform (WPD–HHT) for spindle bearings condition monitoring," *Mech. Syst. Signal Process.*, vol. 33, pp. 197–211, Jul 2012.

[24] R. Li, L. Xu, and L. Yao, "DC fault detection and location in meshed multiterminal HVDC systems based on DC reactor voltage change rate," *IEEE Trans. Power Del.*, vol. 32, pp. 1516–1526, Jul 2016.

[25] A. Hossam-Eldin, A. Lotfy, M. Elgamal, and M. Ebeed, "Artificial intelligence-based short-circuit fault identifier for MT-HVDC systems," *IET Gener. Transm. Distrib.*, vol. 12, pp. 2436–2443, Feb 2018.

[26] M. J. P. Molina, D. M. Larruskain, P. E. López, and A. Etxegarai, "Analysis of local measurement-based algorithms for fault detection in a multi-terminal HVDC grid," *Energies*, vol. 12, p. 4808, Dec 2019.

[27] Q. Huai, K. Liu, A. Hooshyar, H. Ding, L. Qin, and K. Chen, "Line fault location for multi-terminal MMC-HVDC system based on SWT and SVD," *IET Renew. Power Gener.*, vol. 14, pp. 4043–4052, Dec 2020.

[28] M. Farshad, "Fault location in HVDC grids equipped with quick-action protections and circuit breakers based on voltage transient response," *IEEE Trans. Ind. Electron.*, vol. 68, pp. 12881–12889, Dec 2020.

[29] J. Hou, G. Song, P. Chang, R. Xu, and K. S. T. Hussain, "Fault identification scheme for hybrid multi-terminal HVDC system based on control and protection coordination strategy," *Int. J. Electr. Power Energy Syst.*, vol. 136, p. 107591, Oct 2021.

[30] R. K. Singh, S. Agarwal, and V. Verma, "Identification of fault and section identification in multi-terminal HVDC system using unit protection scheme," *Int. J. Syst. Assur. Eng. Manag.*, vol. 13, pp. 1283–1297, Oct 2021.

[31] R. Mardani and M. Z. Ehteshami, "Efficient model-based DC fault detection and location scheme for multi-terminal HVDC systems with voltage source converter," *Electr. Eng.*, vol. 104, pp. 1553–1564, Oct 2021.

[32] E. Tsotsopoulou, X. Karagiannis, T. Papadopoulos, A. Chrysochos, A. Dyśko, and D. Tzelepis, "Protection scheme for multi-terminal HVDC system with superconducting cables based on artificial intelligence algorithms," *Int. J. Electr. Power Energy Syst.*, vol. 149, p. 109037, Feb 2023.